J Mater Sci (2011) 46:6301–6315
DOI 10.1007/s10853-011-5287-0

ABBASCHIAN FESTSCHRIFT

Synthesis of nanocomposites and amorphous alloys by mechanical alloying

C. Suryanarayana · T. Klassen · E. Ivanov

Received: 30 September 2010 / Accepted: 13 January 2011 / Published online: 29 January 2011

Abstract Mechanical alloying (MA) is a powder metallurgy processing technique that involves repeated cold welding, fracturing, and rewelding of powder particles in a high-energy ball mill. Due to the specific advantages offered by this technique, MA was used to synthesize a variety of advanced materials. This article presents two specific examples of synthesis of nanocomposites containing a high volume fraction of the reinforcement phase in Al and TiAl matrices. It was possible to uniformly disperse 50 vol% of nanometric (50 nm) Al_2O_3 in Al and achieve high strength and modulus of elasticity. Similarly, it was possible to disperse 60 vol% of Ti_5Si_3 phase in the γ-TiAl intermetallic. Fully consolidated material showed superplastic behavior at 950 °C and a strain rate of 4×10^{-5} s^{-1}. Amorphous phases were produced by MA of blended elemental powder mixtures in several Fe-based compositions. From the systematic investigations carried out, it was possible to deduce the criteria for glass formation and understand the interesting phenomenon of mechanical crystallization. By conducting some controlled experiments, it was also possible to explain the mechanism of amorphization in these mechanically alloyed powder blends. Other examples of synthesis of advanced materials, e.g., photovoltaic materials and energetic materials, have also been briefly referred to. This article concludes with an indication of the topics that need special attention for further exploitation of these materials.

C. Suryanarayana (✉)
Department of Mechanical, Materials and Aerospace Engineering, University of Central Florida, Orlando, FL 32816-2450, USA
e-mail: csuryana@mail.ucf.edu

C. Suryanarayana
Department of Mechanical Engineering, King Fahd University of Petroleum & Minerals, Dhahran 31261, Saudi Arabia

T. Klassen
Institute of Materials Technology, Helmut-Schmidt-University, Holstenhofweg 85, 22043 Hamburg, Germany

E. Ivanov
Tosoh SMD, Inc., 3600 Ganz Road, Grove City, OH 43213-1895, USA

Introduction

Advanced materials are defined as those where first consideration is given to the systematic synthesis and control of the crystal structure and microstructure of materials to provide precisely tailored properties for demanding applications [1]. With the rapid advances taking place in the technology sectors, there has been a great demand for materials that are stronger, stiffer, lighter, useful at higher temperatures, and less expensive than the existing and available materials. Thus, the high-tech industries have given fillip to efforts in developing novel materials that will perform better for demanding applications. Some of the advanced materials developed during the past few decades include metallic glasses [2, 3] (including the relatively recently developed bulk metallic glasses [4]), quasicrystals [5, 6], high-temperature superconductors, superhard carbonitrides, thin-film diamond synthesis, and nanostructured materials [7–9]. A number of new techniques for processing and characterization of materials have also been developed toward achieving this goal. But, a common underlying principle in obtaining advanced materials has been to process the materials under far-from-equilibrium conditions, i.e., the materials developed are mostly in a metastable or non-equilibrium condition. Turnbull [10] has

coined the phrase "energize and quench" to describe these processes. It is through such processes that the constitution and microstructure of materials can be drastically altered to achieve the desired properties. Some of these "non-equilibrium processing" techniques include rapid solidification processing from the melt, mechanical alloying, laser processing, plasma processing, spray forming, physical and chemical vapor deposition techniques, ion mixing, among others. The relative advantages and disadvantages of these techniques have been discussed in the literature (see, for example, Ref. 11). However, in this article we will describe some of the advanced materials that have been developed using the technique of mechanical alloying.

The process of mechanical alloying

Mechanical Alloying (MA) is a process that was developed by John Benjamin of INCO International in the late 1960s to produce oxide dispersion-strengthened (ODS) materials [12]. The process can be described as a high-energy milling process in which powder particles are subjected to repeated cold welding, fracturing, and rewelding [13, 14]. The generally accepted explanation for alloying to occur from blended elemental powders and formation of different types of phases is that a very fine and intimate mixture of the components (often lamellar if the constituent elements are sufficiently ductile) is formed after milling, if not the final product. The crystalline defects introduced into the material (grain boundaries, interfaces, dislocations, stacking faults, vacancies, and others), which act as fast diffusion paths, and a slight rise in the powder temperature during milling as a result of frictional forces and impact of the grinding balls against other balls and the surfaces of the container were found to facilitate alloy formation. If the final desired phase had not formed directly by MA, then a short annealing treatment at an elevated temperature was found to promote diffusion and consequently alloy formation. Accordingly, it was shown that by a proper choice of the process parameters during MA and choosing an appropriate alloy composition, it is possible to produce a variety of stable and metastable alloys. The thermodynamic criterion that the phase with the lowest free energy would be the most stable phase has been found to be valid in the case of alloy phases synthesized under the continuous deformation conditions as obtained during MA. Some of the significant attributes of MA, not possible to achieve by other processes include (i) formation of alloys at relatively low temperatures, (ii) ability to alloy (and even form metallic glasses) between metals with positive heats of mixing, and (iii) uniform dispersion of a large volume fraction of fine second-phase particles in metallic matrices.

The effects of MA could be categorized under two groups:

1. Constitutional changes: Milling of the blended elemental powders could lead to the formation of solid solutions (both equilibrium and supersaturated), intermetallic phases (equilibrium, metastable and quasicrystalline), and amorphous (or glassy) phases in alloy systems. The actual type of phase formed is dependent on the alloy system, its composition, and the milling conditions employed.
2. Microstructural changes: As a result of MA, the processed materials could develop ultrafine-grained and nanostructured phases.

In many cases, chemical reactions have also been found to take place leading to the formation of novel materials and microstructures. Such a process has been referred to as mechanochemical processing [15]. All these attributes of MA have been well documented in the literature [13, 14, 16].

Even though MA was initially developed to produce ODS nickel-based superalloys and steels for high-temperature applications, in recent years, starting from about 2001, there has been a reemergence of the quest for new applications of the MA materials, not only as structural materials, but also for chemical and functional applications such as catalysis and hydrogen storage, with the realization that contamination of the milled powders is the limiting factor in the widespread applications of the MA materials. Innovative techniques to consolidate the MA powders to full density while retaining the metastable phases (including glassy phases and/or nanostructures) in them were also developed. All these are continuing with the ongoing investigations to enhance the scientific understanding of the MA process. In this article, we will focus on our recent activities and results in the general area of MA in developing advanced materials. As typical examples, we would like to discuss two specific topics:

(1) Development of homogeneously dispersed high volume fraction nanocomposites,
(2) Synthesis of metallic glasses in Fe-based systems.

Synthesis and characterization of photovoltaic materials and energetic materials are also discussed.

High volume fraction nanocomposites

Achievement of a uniform distribution of the reinforcement in a matrix is essential to achieving good mechanical properties of the composites. Further, the mechanical properties of the composite tend to improve with increasing volume fraction and decreasing particle size of the

reinforcement [17]. Traditionally, a reasonably large volume fraction of the reinforcement could be added, if the size of the reinforcement is large (on a micrometer scale). But, if the reinforcement size is very fine (of nanometer dimensions), then the volume fraction added is limited to about 2–4%. This is because the fine powders tend to float to the top of the melt during processing of the composites through solidification processing. However, if we are able to introduce a large volume fraction of nanometer-sized reinforcement, the mechanical properties of the composite are likely to be vastly improved. One of the main challenges in achieving a homogeneous distribution of the nanometric ceramic phase in the metal matrix is agglomeration of the reinforcement particles. This becomes even more significant when the size of the reinforcement is small and its volume fraction is high. In our investigations, during the past few years, we have successfully achieved a very uniform distribution of the reinforcement phases in different types of matrices through the solid-state powder processing technique of MA [18–27]. These include homogeneous dispersion of lead in Al and Al–Cu alloys [18], graphite in an Al-6061 alloy matrix [19], effect of clustering of the reinforcement on the mechanical properties of the composites [20], dispersion of a high volume fraction of Al_2O_3 in Al [21], and of Ti_5Si_3 in γ-TiAl [22–24], synthesis of $MoSi_2 + Si_3N_4$ composites for high-temperature applications [25, 26], and synthesis of amorphous + intermetallic composites in Al–Mg alloys [27]. However, in this article, we will describe our new results obtained in two systems.

Al–Al_2O_3 composites

Aluminum-based metal matrix composites are ideal materials for structural applications in the aircraft and automotive industries due to their lightweight and high strength-to-weight ratio. Reinforcement of the ductile aluminum matrix with stronger and stiffer second-phase reinforcements like oxides, carbides, borides, and nitrides provides a combination of properties of both the metallic matrix and the ceramic reinforcement. Uniform dispersion of the fine reinforcements, especially at large volume fractions, and a fine grain size of the matrix contribute to improving the mechanical properties of the composite.

Most of the study carried out to date on discontinuously reinforced aluminum was primarily concerned with dispersing reinforcements on the micrometer scale (a few to a couple of hundred micrometers). Even though studies were carried out on nanometer-sized reinforcements, the volume fraction of the reinforcements was very small. Thus, there is a gap in understanding the structure and properties of high volume fraction composites containing nanometer-sized reinforcements. Therefore, we have conducted investigations to synthesize and characterize Al–Al_2O_3 composites with the Al_2O_3 reinforcement varying in size from 50 nm to 5 μm, and the volume fraction from 5 to 50%. The reasons behind the choice of this combination of particle sizes and volume fractions were to check (i) whether there is a maximum volume fraction of Al_2O_3 beyond which it will be difficult to achieve a uniform distribution in the matrix and to consolidate the material to full density, and also (ii) to see if there is a minimum particle size, below which again it will be difficult to achieve a uniform distribution of the two components in the composite.

The starting materials were pure Al powder of about 45 μm size and 99.8% purity and Al_2O_3 powders 50 nm, 150 nm, and 5 μm sizes with 99.99% purity. The volume fraction of Al_2O_3 was 5, 10, 20, 30, and 50%. Milling was conducted in a SPEX 8000 mixer mill using hardened stainless steel balls and a ball-to-powder weight ratio (BPR) of 10:1. Loading and unloading of the powders was done in an evacuated and argon-filled glove box. A small quantity (0.5–1.0 wt%) of the stearic acid was used as a process control agent to prevent excessive cold welding of the powder particles among themselves, on to the internal surfaces of the vial, and to the surface of the grinding medium during milling. The milled powders were taken out from the milling vial at regular intervals of 5, 10, 15, and 20 h for microstructural characterization through optical and scanning electron microscopy (SEM) methods and crystal structure analysis using X-ray diffraction (XRD) methods.

Microstructural observations suggested that the distribution of Al_2O_3 particles in the Al matrix was uniform after 20 h of milling. This was true in almost all the cases investigated. Figure 1 shows that a very uniform dispersion of the fine 50-nm Al_2O_3 particles was achieved even when the volume fraction of the reinforcement was 50%. This corresponds to the finest particle size and largest volume fraction, the maximum value achieved so far in any nanocomposite. Similar uniform distributions were obtained in the larger size and smaller volume fractions of the reinforcement also. Since the uniform distribution of the Al_2O_3 particles in the matrix may not be detected at this resolution, X-ray elemental mapping was conducted in the SEM. Figure 2 clearly shows that a uniform distribution of the reinforcement phase was obtained as revealed by the uniform distribution of the spots in the aluminum and oxygen dot maps [21].

An interesting observation made during this study was that the stable γ-Al_2O_3 transformed to α-Al_2O_3 on milling, when the Al_2O_3 powder particle size was small, e.g., 50 nm [28]. However, no such transformation occurred when the Al_2O_3 particle size was large, e.g., 5 μm. This was explained on the basis of a large surface-to-volume ratio of

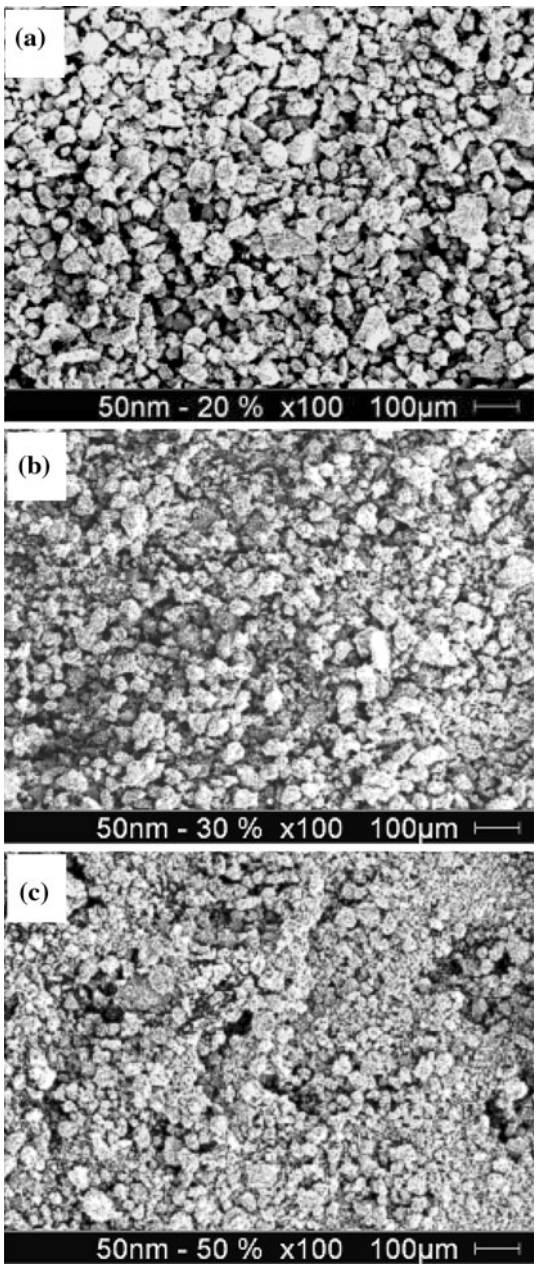

Fig. 1 SEM micrographs of Al–Al_2O_3 (50 nm) powders milled to the steady-state condition (20 h) showing a uniform distribution of Al_2O_3 in the Al matrix. **a** 20 vol%, **b** 30 vol%, and **c** 50 vol% Al_2O_3

small-sized particles. Another observation was that such a transformation occurred easily when the γ-Al_2O_3 powder particle contained a small amount of the α-phase, which acted as a seed for the growth of the α-phase.

These composites with a large volume fraction of the reinforcement of the Al_2O_3 powders were very hard and strong and consequently it was not easy to consolidate them to full density by any single different technique that is presently available. Therefore, to determine the effect of reinforcement particle size and volume fraction, nanocomposites with 50 nm and 150 nm particle size and 5 and 10 vol% were consolidated to full density. Even though vacuum hot pressing and hot isostatic pressing were tried individually, it was difficult to achieve high density by either of the methods alone. Close to 100% of the theoretical density was achieved only by a combination of vacuum hot pressing followed by hot isostatic pressing [29]. Compression testing was done on the fully dense samples, and the strength properties and modulus values were determined. Table 1 lists the mechanical properties of these composites. Figure 3 shows the variation of the modulus of elasticity as a function of the Al_2O_3 content. From these results, it may be noted that the strength and modulus increased with (i) increasing volume fraction and (ii) decreasing size of the reinforcement. Comparison of these modulus values with those calculated using the iso-strain and iso-stress conditions suggested that composites with the smaller reinforcement particle size (50 nm) behaved closer to the iso-strain condition, while composites with the larger reinforcement size (150 nm) behaved closer to the iso-stress condition. This observation clearly suggests that it is possible to tailor the modulus (and strength) of the nanocomposites by choosing the appropriate reinforcement size and volume fraction. Such a processing methodology should be equally applicable to other systems, even though the details of processing and consolidation would be different.

Neutron diffraction studies were also conducted on these Al–Al_2O_3 nanocomposites with the idea of determining the load redistribution between the matrix and reinforcement phases. For this purpose, neutron diffraction patterns have been recorded at different stress levels, and the strain in the different planes of the matrix (Al) and the reinforcement (Al_2O_3) were determined by measuring the shift in the positions of the diffraction peaks. From these values, the stress–strain plots were made and the modulus values were determined. It was noted that the modulus of elasticity of the matrix phase increases after macroscopic yielding, while it decreases in the reinforcement phase. These observations clearly suggest that the matrix is bearing more load than the reinforcement [30].

TiAl–Ti_5Si_3 composites

Lightweight intermetallic alloys based on γ-TiAl are promising materials for high-temperature structural applications, e.g., in aircraft engines or stationary turbines [31, 32]. Even though they have many desirable properties such as high specific strength and modulus both at room and elevated temperatures, and good corrosion and oxidation resistance, they suffer from inadequate room temperature ductility and insufficient creep resistance at elevated temperatures, especially between 800 and 850 °C, an important requirement for elevated temperature applications of

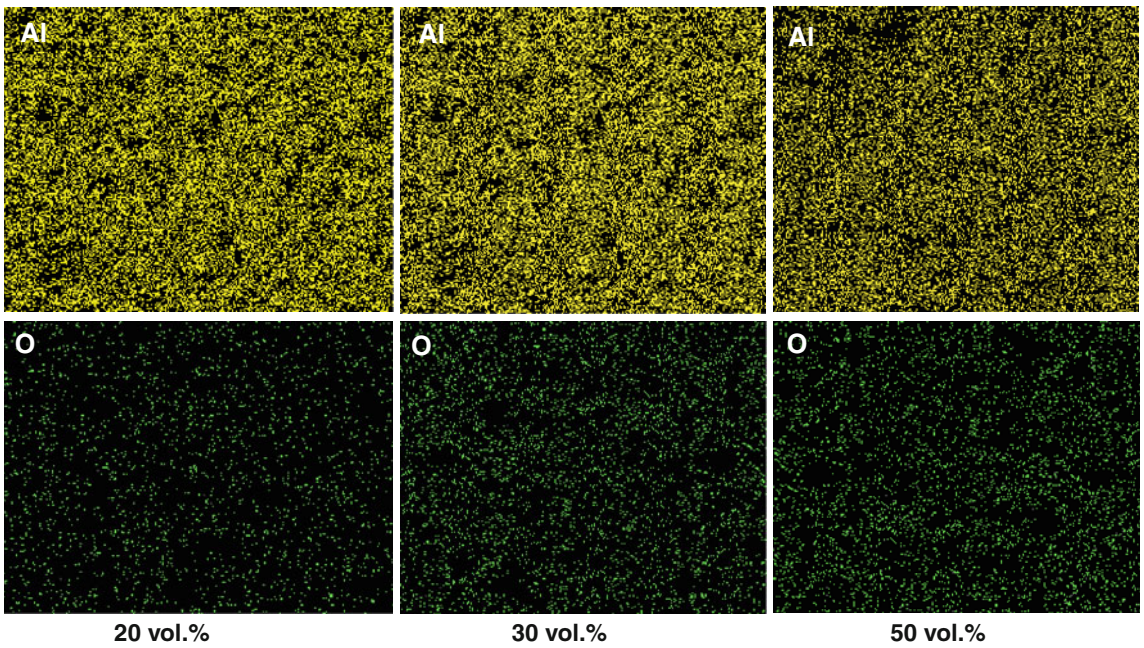

Fig. 2 X-ray maps showing distribution of Aluminum (*top*) and Oxygen (*bottom*) atoms in the Al–Al_2O_3 (50 nm) powders milled for 20 h

Table 1 Mechanical properties of Al–Al_2O_3 nanocomposites obtained by milling and subsequent consolidation by vacuum hot pressing and hot isostatic pressing

Al_2O_3		Yield strength (MPa)	Compressive strength (MPa)	Elastic modulus (GPa)	Elastic modulus calculated by the rule of mixtures[a] (GPa)
Particle size (nm)	Volume fraction (%)				
50	5	488	605	78	83
50	10	515	628	90	95
150	5	409	544	75	83
150	10	461	600	77	95

[a] $E_c = V_m E_m + V_r E_r$ where E and V represent the elastic modulus and volume fraction, respectively, and the subscripts c, m, and r represent the composite, matrix, and reinforcement, respectively

these materials. Therefore, current research programs have been addressing the development of high-temperature materials with adequate room temperature ductility for easy formability and ability to increase the high-temperature strength by a suitable heat treatment or alloying additions to obtain sufficient creep resistance.

It has been shown that the compressive strength of binary γ-TiAl alloys with nanometer-sized grains is about 2600 MPa at room temperature and that, at temperatures higher than about 500 °C, the strength drops very rapidly to low values [33, 34]. In fact, the strength was found to decrease at a faster rate for ultrafine-grained materials than for the coarse-grained counterparts. That is, the smaller the grain size of the specimen, the stronger and sharper is the drop in yield strength at elevated temperatures. This observation suggests that monolithic nanostructured materials may not be suitable for achieving the desired creep resistance.

The Ti–Al–Si alloy system was chosen because it is a model system to study the influence of phase distribution and microstructure on the high-temperature deformation behavior of ceramic–intermetallic composites. Earlier study has demonstrated that favorable deformation behavior could be obtained in nanostructured/submicron-sized TiAl-based intermetallics. Thus, it was decided to check whether the microstructure has a similar influence on the mechanical behavior of *ceramic-based* ceramic-intermetallic composites which could then lead to easy deformability and eventually the possibility of achieving superplasticity. It is possible that the creep properties of these composites will be poor at low temperatures, but, similar to that in TiAl-based alloys, it could be improved through grain coarsening after deformation at elevated temperatures.

Composites of γ-TiAl and ξ-Ti_5Si_3 phase, with the volume fraction of the ξ-Ti_5Si_3 phase varying from 0 to

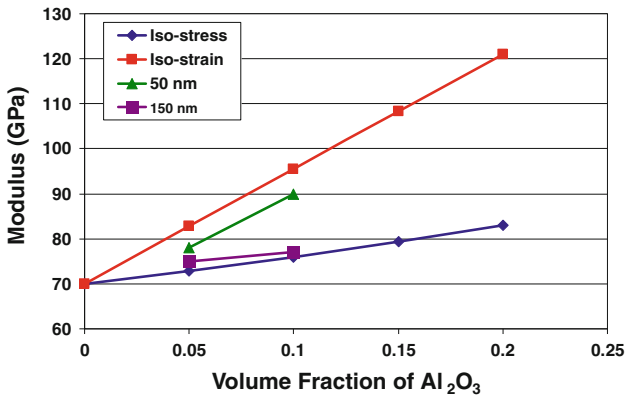

Fig. 3 Variation of modulus of elasticity with volume fraction of Al_2O_3 for two different particle sizes (50 and 150 nm). The *solid lines* were drawn on the basis of iso-stress or iso-strain conditions using the rule of mixtures. Note that the variation is close to the iso-strain condition for 50 nm-size Al_2O_3 particles and close to the iso-stress condition for the 150 nm-size Al_2O_3 particles

60 vol%, were produced by MA of the blended elemental powders. Fully dense and porosity-free compacts were produced by hot isostatic pressing, with the resulting grain size of each of the phases being about 400 nm. Figure 4 shows scanning electron micrographs of the γ-TiAl + 60 vol% ξ-Ti_5Si_3composite showing that the two constituent phases are of sub-micron grain size and that they are very uniformly distributed throughout the microstructure. Grains with annealing twins inside them belong to the γ-TiAl phase and the other grains belong to the Ti_5Si_3 phase. Such a microstructure is expected to be conducive to superplastic deformation behavior. To test this hypothesis, both compression and tensile testing of these composite specimens were conducted at different temperatures and strain rates [24]. From the tensile stress–strain plots of the γ-TiAl + 60 vol% ξ-Ti_5Si_3 composite specimens, we could draw the following conclusions:

First, the strength decreased with increasing temperature and decreasing strain rate, both expected from normal mechanical behavior of metallic materials. Secondly, the specimens tested at 950 °C and a strain rate of 4×10^{-5} s^{-1} and 1000 °C and a strain rate of 4×10^{-4} s^{-1} exhibited large ductilities of nearly 150 and 100%, respectively. Considering that this composite is based on a ceramic material (Ti_5Si_3) this is a very high amount of deformation, suggestive of superplastic deformation. Final proof is provided by TEM investigations that confirm the continued stability of the microstructure after deformation. Thirdly, even though the strain rate employed is relatively low, it is interesting that superplasticity was observed at 950 °C, corresponding to about 0.5 T_m, where T_m is the melting temperature of the alloy. This should be compared with the coarse-grained γ-TiAl material which shows the superplastic behavior only at temperatures about 300–400 °C higher than

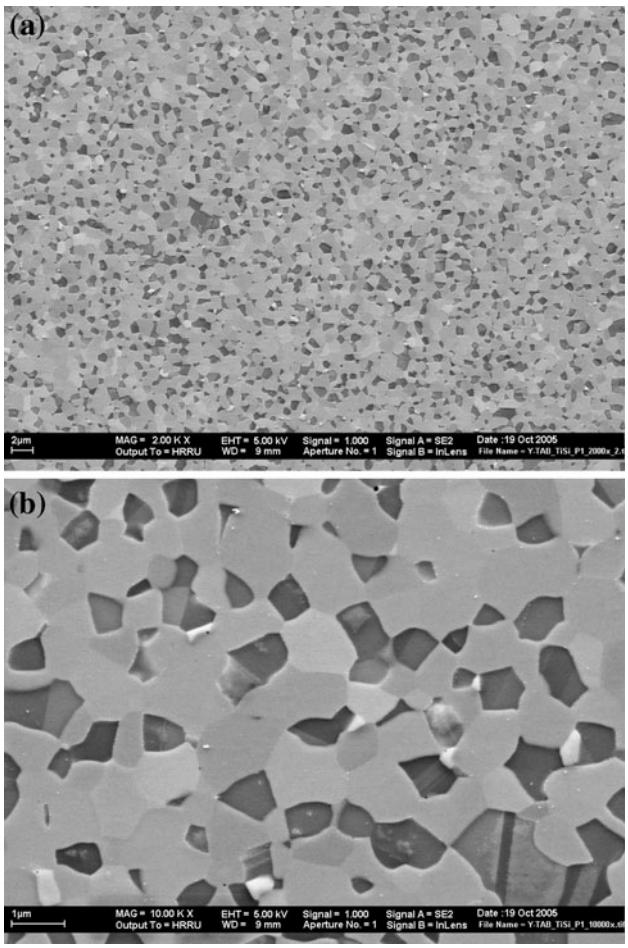

Fig. 4 Scanning electron micrographs of the γ-TiAl + 60 vol% ξ-Ti_5Si_3 composite specimen showing that the two phases are very uniformly distributed in the microstructure. Such a microstructure is conducive to observing superplastic deformation under appropriate conditions of testing. **a** Low magnification and **b** High magnification

the temperature observed in this investigation [23, 35]. Figure 5 shows photographs of the actual specimens before and after tensile testing, showing significant amounts of elongation in the samples.

Glass formation in Fe-based alloy systems

Metallic glasses have an interesting combination of mechanical, physical, and chemical properties. They have been produced in several alloy systems by many different techniques. But, the most commonly used technique has been rapid solidification processing (RSP) [2, 3, 36, 37]. As is well known, the critical cooling rate for glass formation needs to be exceeded so that formation of the crystalline nuclei could be avoided for the glass to form. However, since this is an experimentally determined value (and is time-consuming and also difficult to measure), several

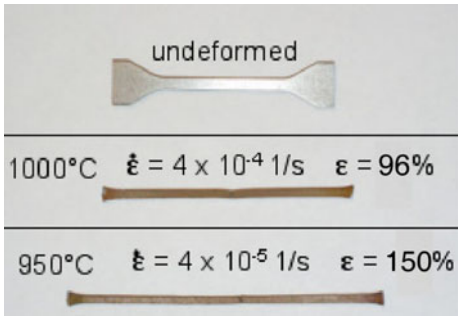

Fig. 5 Photographs of the actual tensile specimens before and after tensile testing

other empirical criteria have been proposed to explain glass formation in alloy systems [2–4]. Two most commonly used criteria have been (a) a high reduced glass transition temperature, $T_{rg} = T_g/T_l$, where T_g is the glass transition temperature and T_l is the liquidus temperature of the alloy, and (b) presence of deep eutectics in the phase diagrams.

The development of bulk metallic glasses in the late 1980s [4, 38] has attracted the attention of materials scientists all over the world. Three criteria were proposed for the formation of bulk metallic glasses, viz., (a) presence of at least three components in the alloy system, (b) atomic radius difference of >12% between the constituent elements, and (c) negative heat of mixing among the constituent elements. A very large number of bulk metallic glasses were produced using this set of criteria. But, since 2003 a number of new criteria based on the thermal properties of the alloys and physical characteristics of the component atoms were developed. These include the so-called α, β, γ, γ_m, δ, σ, etc. parameters. In spite of this large number of parameters, the predictabilities of glass formation have not significantly improved [39] and it has been difficult to exactly specify which alloy compositions would produce the glassy phases. But, it is important to remember that all these criteria have been developed for metallic glasses processed via the solidification route. As mentioned earlier, MA, a completely solid-state powder processing technique, is another important technique to produce amorphous alloys. However, there have not been any systematic investigations to study the conditions under which amorphous phases are formed by MA. Therefore, we wished to determine if the criteria applicable to RSP studies would be applicable to the solid-state processed amorphous alloys or other criteria need to be formulated to predict glass formation in alloy systems processed by MA. For this purpose, we had undertaken a comprehensive investigation on the glass formation behavior and stability of several Fe-based glassy alloys synthesized by MA.

Blended elemental (BE) pure metal powders (of >99.9% purity) were weighed out corresponding to the generic composition of $Fe_{42}X_{28}Zr_{10}B_{20}$ (where the subscripts represent the composition of the alloy in atomic percentage and X = Al, Co, Ge, Mn, Ni, or Sn). Other alloying elements such as Nb and C have also been added to the above compositions in some investigations. In addition, a multi-component Fe-based alloy composition has also been investigated. MA was carried out in a SPEX CertiPrep 8000 D shaker mill. For each experiment, 10 g of the blended elemental powder mix and 100 g of hardened stainless steel balls were loaded into the milling container, thus maintaining a BPR of 10:1 during milling. About 1 wt% of stearic acid was added as a process control agent to prevent severe agglomeration of the powder to the vial walls and/or the grinding medium. The phase evolution during milling was monitored by XRD using a Rigaku X-ray diffractometer with CuKα radiation (λ = 0.15406 nm) at 40 kV and 35 mA settings. The XRD patterns were recorded in the 2θ range of 30–90° and analyzed using standard procedures [40].

Criterion for glass formation

The element X in the general alloy composition $Fe_{42}X_{28}Zr_{10}B_{20}$ was selected based on the number of intermetallics it forms with Zr under equilibrium conditions at room temperature [41]. This number increases from 1 with Mn to 8 with Al, which provides a basis to analyze the results systematically. Further, the negative heat of formation of the intermetallics with Zr is much higher than that with either Fe or B [42]. Thus, the probability of forming an intermetallic with Zr during milling is higher than with Fe or B.

Figure 6 presents the XRD patterns showing the structural evolution in the blended elemental powder mixtures of $Fe_{42}Al_{28}Zr_{10}B_{20}$ and $Fe_{42}Co_{28}Zr_{10}B_{20}$ compositions as a function of milling time. While all the expected diffraction peaks of Fe, Al, and Zr are seen in the as-blended powder mixture of $Fe_{42}Al_{28}Zr_{10}B_{20}$, peaks from boron are not seen probably because of its low scattering factor. On milling the powder mix for 20 h, it is noted that amorphization had occurred, as evidenced by the presence of a broad diffuse peak centered at the $(110)_{Fe}$ position. On further milling (say, for 50 h), however, this diffuse peak started becoming sharp, and additional low-intensity peaks started appearing. This process, referred to here as mechanical crystallization, will be discussed later in some detail. The sequence of phase formation on milling the powders was different depending on the alloy system. It may be noted that while an amorphous phase had formed on milling the $Fe_{42}Al_{28}Zr_{10}B_{20}$ powder blend for 20 h, amorphization did not occur in the $Fe_{42}Co_{28}Zr_{10}B_{20}$ powder blend.

The phase formation sequence in all the six powder blends can be summarized into three groups as follows:

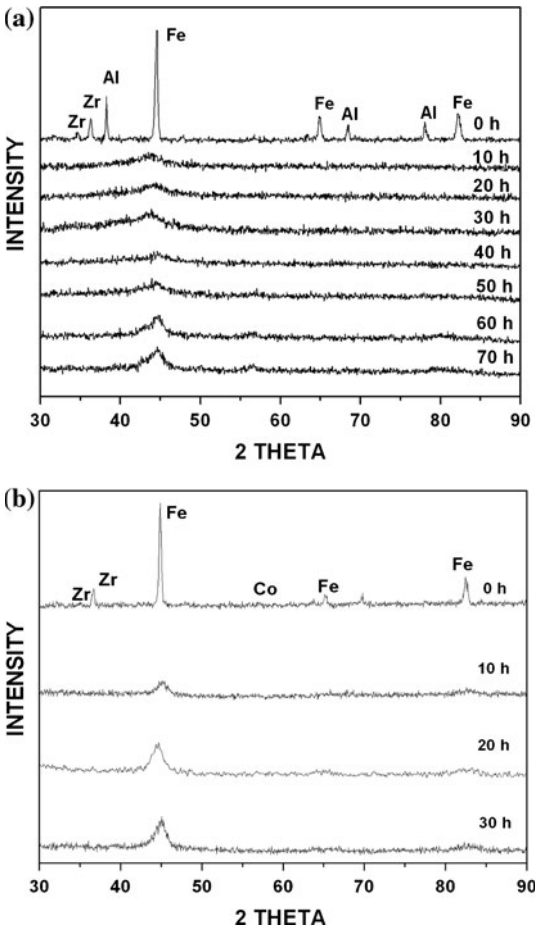

Fig. 6 Structural evolution in the blended elemental powder mix of **a** $Fe_{42}Al_{28}Zr_{10}B_{20}$ and **b** $Fe_{42}Co_{28}Zr_{10}B_{20}$ as a function of milling time. Note that the amorphous phase had started to form on milling for about 10 h and was stable up to about 40 h in the $Fe_{42}Al_{28}Zr_{10}B_{20}$alloy system. An amorphous phase did not form in the $Fe_{42}Co_{28}Zr_{10}B_{20}$alloy system. Instead, a solid solution was the final phase to form in this alloy system

(1) BE powder → Intermetallics → Solid solution

Examples: Mn- and Sn-containing systems,

(2) BE powder → Solid solution

Example: Co-containing system,

(3) BE powder → Intermetallics → Amorphous phase → (Mechanical) Crystallization

Examples: Al-, Ge-, and Ni-containing systems.

The time required for amorphization, which can be considered a measure of the glass-forming ability (GFA) of the alloy, is also different for different powder blends. Table 2 summarizes the results obtained, including the equilibrium number of intermetallic phases present between X and the constituent elements (Zr, Fe, or B) in the powder bend [43]. A close examination of Table 2 clearly reveals that the ease of amorphization (i.e., GFA) increased with the number of intermetallics present in the constituent Zr-X binary phase diagrams. This is apparent from the powder blends containing Al or Ni, which amorphized in 10 or 20 h, respectively. While the quaternary Fe–Zr–Al–B contains eight intermetallic phases in the binary system between Zr and Al, the Fe–Zr–Ni–B system contains seven intermetallic phases in the binary system between Zr and Ni. Similarly, the Ge-containing system which also amorphized in 10 h, contains five intermetallic phases between Zr and Ge. The Zr–Co, Zr–Mn, and Zr–Sn systems which did not show amorphization on milling contain five, one, and three intermetallic phases, respectively. However, when we consider the total number of intermetallic phases, it can be clearly seen that the systems which amorphized on milling contain $\geq$10 intermetallic phases in all the constituent binary phase diagrams. If the alloy system contained <10 intermetallic phases, then amorphization was not observed. Note, however, that when the total number of intermetallics is only 10 (with the Ge-containing alloy), the time required for amorphization is only 10 h. But, this is a special case because Ge is a semi-metal with strong directional bonds. Thus, it becomes easier to amorphize alloys containing Ge (or other semi metals). From a critical analysis of the constituent binary phase diagrams, it also becomes clear that when the phase diagrams contain extensive solid solutions, it will be very difficult to amorphize them.

Amorphization by MA occurs when the free energy of the crystalline phase, G_C is higher than that of the

Table 2 Time required for glass formation in $Fe_{42}X_{28}Zr_{10}B_{20}$ alloys and the number of intermetallics in the respective binary alloy systems [43]

Element X	Number of intermetallics between			Total number of intermetallics	Milling time required for amorphization (h)
	X and Zr	X and Fe	X and B		
Al	8	5	2	15	10
Co	5	Nil	3	8	No amorphization
Ge	5	5	Nil	10	10
Mn	1	Nil	5	6	No amorphization
Ni	7	1	4	12	20
Sn	3	2	Nil	5	No amorphization

hypothetical amorphous phase, G_A, i.e., $G_C > G_A$ [44]. A crystalline phase normally has a lower free energy than the amorphous phase. But, its free energy can be increased by introducing a variety of crystal defects such as dislocations, grain boundaries, stacking faults, etc. If an intermetallic has formed, then additional energy can be introduced by disordering the crystal lattice. By this approach, it is then possible to obtain a situation when $G_C + G_D > G_A$, where G_D is the free energy increase due to introduction of defects.

The magnitude of energy increase is different for different types of defects. As an example, increasing the dislocation density to $10^{16}/m^2$ increases the free energy by about 1 kJ/mol, while decreasing the grain size down to 1 nm increases the free energy by about 10 kJ/mol [45]. The only way a solid solution could contribute to an increase in the energy of the system is by grain refinement. But, this increase in energy is not sufficiently high to amorphize the system [45]. On the other hand, the presence of intermetallics in an alloy system significantly increases the energy contributing to amorphization. This is due to two important effects. First, disordering of intermetallics contributes an energy of about 15 kJ/mol of atoms to the system. For example, in strongly ordered intermetallics such as NiAl and γ-TiAl that continue to be in the ordered state till melting, the disordering energy has been estimated to be about 17.5 kJ/mol [46]. Secondly, a slight change in the stoichiometry of the intermetallic increases the free energy of the system drastically. In addition, grain size reduction contributes about 5 kJ/mol. Further, disordering of intermetallics has also been shown to be possible by heavy deformation [47]. Since MA reduces the grain size to nanometer levels and also disorders the usually ordered intermetallics, the energy of the milled powders is significantly raised. In fact, it is raised to a level above that of the hypothetical amorphous phase. This condition leads to a situation where the preferential formation of the amorphous phase is favored over the crystalline phase.

Phase diagram features have been used to predict glass formation by RSP and other methods as well. For example, since alloys with high T_{rg} values are known to be good glass formers, and alloys in the vicinity of deep eutectics exhibit high T_{rg} values, deep-eutectic alloy compositions have been shown to exhibit high GFA [48]. Further, elemental solids exhibiting a large number of polymorphic phases have been shown to exhibit higher GFA than elements that do not have a large number of polymorphs [49]. In contrast, amorphous phases are obtained mostly around equiatomic compositions by the MA methods. Also, the composition range for amorphous phase formation is much wider in alloys produced by MA than in those obtained by RSP [13, 14]. Difficulty in amorphization has been observed with RSP in alloys having melting maxima, too many peritectic reactions, high-temperature eutectics and also alloys having positive heats of mixing. However, amorphization has been observed in most of these cases by MA [13, 14]. Further, it was observed that it is not possible to transform very dilute alloys (with low concentration of solute atoms) to the amorphous state by MA methods [50], whereas solute contents of as low as 9 at% were found sufficient for glass formation in Fe–Zr and Co–Zr alloy systems by RSP methods [51]. Thus, even though phase diagrams are useful guidelines in choosing alloy compositions for easy glass formation by both the methods, the features to look for appear to be quite different for the RSP and MA methods. It is just fortuitous that some alloy compositions can be amorphized by both the methods.

Thus, these observations provide a simple and visual means of identifying alloy systems which are likely to become amorphous on subjecting them to milling. If the equilibrium phase diagrams show the presence of a room temperature solid solution phase over a wide composition range, then amorphization is not easy. On the other hand, if the phase diagram contains a large number of intermetallic phases, then amorphization is a possibility.

Mechanical crystallization

It was briefly mentioned in the previous section that an amorphous phase transforms into a crystalline phase on continued milling, and that this phenomenon was referred to as mechanical crystallization. This is a very unusual process and has lot of potential applications in alloy design approaches since it will be possible to produce the alloy in either a fully amorphous, amorphous + nanocrystalline composite, or a completely crystalline state with different grain sizes, depending upon the time of milling or the temperature and time of annealing of the amorphous alloy.

Figure 7a shows the XRD patterns of the blended elemental powder of the composition $Fe_{42}Ge_{28}Zr_{10}B_{20}$ mechanically milled for 10 and 60 h. One may note the significant change in the XRD patterns. While the pattern at 10 h of milling clearly shows the presence of an amorphous phase, the pattern at 60 h of milling shows the presence of a crystalline phase, superimposed over the broad and diffuse halo, characteristic of the amorphous phase. By analyzing the sharp diffraction peaks, it was possible to establish that the crystalline phase corresponds to the BCC structure with the lattice parameter $a = 0.2878$ nm, suggesting that this is an α-Fe solid solution containing the solute elements present in the powder blend. Primary crystallization of metallic glasses produced by RSP methods was shown to produce a crystalline solid solution phase coexisting with an amorphous phase, which has a composition different from that of the initial amorphous phase [52]. Thus, formation of the α-Fe phase in our

MA powder may be interpreted to be a result of primary crystallization occurring in the amorphous alloy.

Figure 7b shows the XRD patterns of the $Fe_{42}Ni_{28}Zr_{10}C_{10}B_{10}$ powder blend milled for 8 and 30 h. Similar to Fig. 7a, the powder milled for 8 h is fully amorphous and the same powder milled for 30 h shows the presence of sharp crystalline peaks superimposed over the amorphous phase. But, the important difference between Fig. 7a and b is that while the crystalline phase is the α-Fe solid solution in Fig. 7a, it is a mixture of crystalline phases in Fig. 7b. Thus, the sequence of phase formation in these powders during milling is that the blended elemental powder first forms intermetallic phases, then an amorphous phase, and eventually mechanical crystallization occurs resulting in the formation of crystalline phase(s).

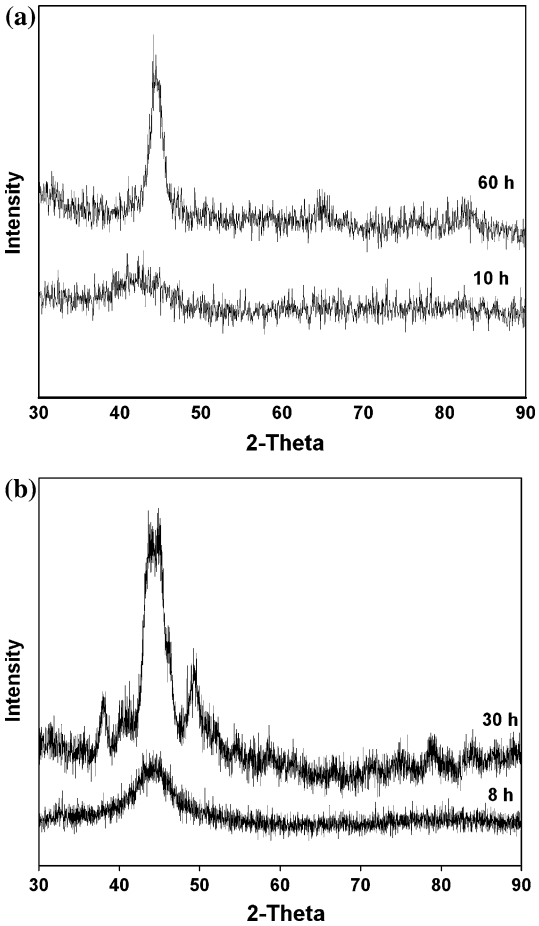

Fig. 7 **a** X-ray diffraction patterns of the $Fe_{42}Ge_{28}Zr_{10}B_{20}$ powder blend milled for 10 and 60 h. While the powder milled for 10 h shows the presence of an amorphous phase, the powder milled for. 60 h shows the presence of a crystalline phase. **b** X-ray diffraction patterns of the $Fe_{42}Ni_{28}Zr_{10}C_{10}B_{10}$ powder blend milled for 8 and 30 h. Note that the powder milled for 8 h shows the presence of an amorphous phase. On continued milling of this powder containing the amorphous phase to 30 h, mechanical crystallization had occurred resulting in the formation of several crystalline phases

Mechanical crystallization processes have also been observed in other alloy systems that formed the amorphous phase on MA [53–55]. In fact, it is now becoming apparent that this phenomenon of mechanical crystallization is not as rare as it was once thought to be [56]. There can be many reasons for the formation of a crystalline phase after the formation of an amorphous phase during MA. The important factors could be (1) rise in temperature to a level above that of the crystallization temperature of the amorphous alloy [13, 14], (2) powder contamination due to which a stable crystalline impurity phase forms [57], (3) phenomenon of inverse melting [58], and (4) basic thermodynamic considerations. It now appears clear that basic thermodynamic stabilities of the different phases under the conditions of milling are responsible for mechanical crystallization. This can be further explained with reference to a free energy versus composition diagram.

Figure 8 is a schematic diagram showing the variation of free energy with composition for the Fe-based alloy systems investigated here. The possible (stable and metastable) constitution in this system is (a) blended elemental (BE) powder mixture, (b) α-Fe, the solid solution of all the alloying elements in Fe, (c) an amorphous phase, (d) intermetallic phases, and (e) different combinations of these phases. The stability of any phase will be determined by its relative position in the free energy plot—the lower the free energy the more stable the phase is. Since it is possible to have a large number of intermetallic phases in this multicomponent system, and since it is difficult to

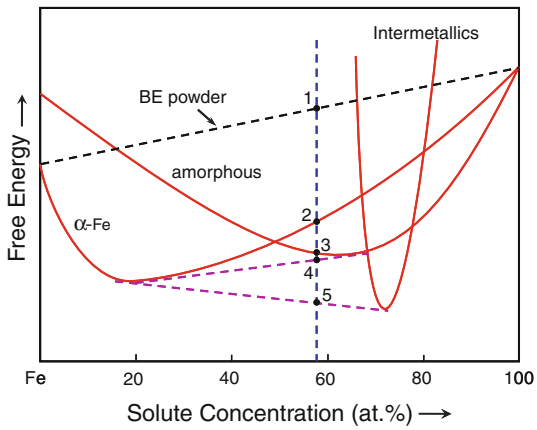

Fig. 8 Hypothetical free energy versus composition diagram to explain the mechanism of mechanical crystallization in the $Fe_{42}X_{28}Zr_{10}C_{10}B_{10}$ system. Note that point "1" represents the free energy of the blended elemental powders. Similarly, point "2" represents formation of the α-Fe solid solution containing all the alloying elements in Fe, point "3" formation of the homogeneous amorphous phase, point "4" a mixture of the amorphous phase with a different solute content (amorphous) than at "3" and the solid solution α-Fe with different solute content, and point "5" is for the equilibrium situation when the solid solution and intermetallic phases coexist

indicate each of them separately, for simplicity, all of them are grouped together as "Intermetallics". We will now consider the relative stabilities of the different competing phases in the $Fe_{42}X_{28}Zr_{10}B_{20}$ system. For our discussions here, we have considered all the solute elements together, which make up to 58 at%, as "solute".

The free energy of the BE powder mixture is indicated by point "1", which represents the point of intersection of the composition vertical with the line joining the free energies of pure Fe and the "solute". On milling this powder, a solid solution phase containing all the solute elements in Fe (or a mixture of intermetallics and a solid solution, in some cases) is seen to form and its free energy is indicated by point "2". The solid solution forms because it has a lower free energy than the BE powder mixture. Since MA introduces a variety of crystal defects such as dislocations, vacancies, stacking faults, and grain boundaries, the crystalline phases in the milled powders will contain excess energy. This energy will continue to increase with milling time and reach a value which is above that of the metastable amorphous phase. Thus, the amorphous phase gets stabilized (point "3"). On primary crystallization of the amorphous phase, the new constitution will be a mixture of the α-Fe solid solution or intermetallics and the amorphous phase, which now has a composition different from the original amorphous phase. Further, the new solid solution phase also has a composition different from the original α-Fe phase. The free energy of the mixture of this solid solution and the amorphous phases, indicated by "point 4", will have a free energy lower than that of the amorphous phase. The equilibrium mixture of the α-Fe solid solution and "intermetallics" will have the lowest free energy of all the phase mixtures, as indicated by point "5" in the figure. It may be noted that the process of mechanical crystallization is unique to the MA process and can be achieved only on milling of the amorphous powder.

Mechanism of amorphization

Based on a recent report that addition of an alloying element with a positive heat of mixing with a constituent element in a given alloy system improves the GFA and also the plasticity of the inherently brittle bulk glassy alloy [59], we decided to investigate whether the GFA can be improved in the MA-processed amorphous phases also. Indeed, this should be more favorable during amorphization by the MA methods, since MA of immiscible metals has been known to form amorphous phases [13, 60].

The element Nb was chosen because it exhibits a positive heat of mixing with Zr (+17 kJ/mol) [61]. In addition, Nb has an atomic diameter 0.2936 nm, substantially larger than that of Fe (0.2482 nm) and Ni (0.2492 nm), but smaller than that of Zr (0.3186 nm). Accordingly, we prepared BE powder mixtures of $Fe_{42}Ni_{28}Zr_{10-x}Nb_xB_{20}$ with $x = 1$, 2, 4, and 6 at% Nb. Milling of these powders led to the observation of two important features. The first was that the ease of glass formation was different depending on the Nb content [62]. The highest GFA was achieved in the powder blend with 2 at% Nb. The second, and more interesting, observation was that lattice contraction was observed at the time of amorphization.

Table 3 lists the time necessary for amorphization in the $Fe_{42}Ni_{28}Zr_{10-x}Nb_xB_{20}$ powder mix as a function of Nb content. It may be noted that the time decreases from 20 h in the Nb-free alloy to the minimum value of about 8 h, in the alloy with $x = 2$, suggesting that the GFA was highest at this Nb content. Reduced milling times were observed for amorphization in the other powder blends with $x = 1$, 4, and 6 at% Nb also, noting that the times required for amorphization were different at different Nb contents.

The position of the broad diffuse peak, representing the amorphous phase in the XRD patterns, was measured. To get a better appreciation of the peak shifts, the X-ray broad peaks were fitted to a Gaussian profile. Figure 9 shows the variation of the 2θ values as a function of milling time and for different Nb contents. It is clear from this figure that the position of the $(110)_{Fe}$ peak has shifted with milling time in all the cases, although apparently not in a consistent manner. In the initial stages of milling, the 2θ value decreased suggesting that the lattice parameter has increased, due to formation of an α-Fe solid solution. Since all the substitutional solute elements have an atomic size larger than that of Fe, and B dissolves interstitially, the lattice is expected to dilate and therefore the 2θ value will decrease with milling time. But, with continued milling, this crystalline phase became destabilized resulting in the formation of an amorphous phase.

The interesting observation made was that the 2θ value of the peak increased at the time of amorphization, i.e., lattice contraction had occurred. This observation has been made for the first time, even though this is expected to occur according to theoretical predictions. Formation of the amorphous phase during milling and the associated lattice contraction can be satisfactorily explained on the basis of

Table 3 Time required for amorphization in the $Fe_{42}Ni_{28}Zr_{10-x}Nb_xB_{20}$ powder mix

At% Nb	Time for amorphization (h)
0	20
1	10
2	8
4	10
6	15

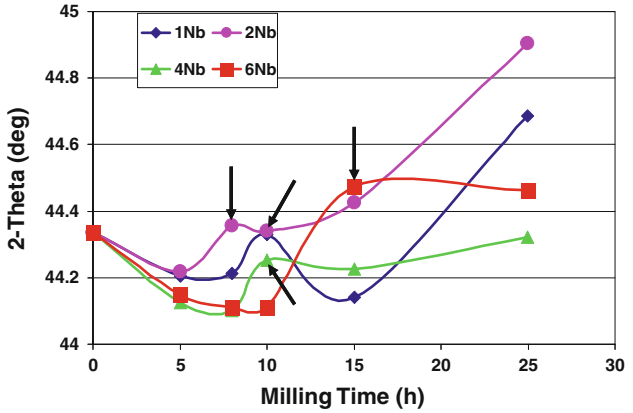

Fig. 9 Variation of the 2-theta values corresponding to the diffuse broad peak with milling time for the different $Fe_{42}Ni_{28}Zr_{10-x}Nb_xB_{20}$ powder blends with $x = 1$, 2, 4, and 6 at% Nb. The *arrow* corresponds to the time when the amorphous phase formation has been observed

the atomic strain model of Egami and its subsequent development by Miracle and co-workers.

Egami and Waseda [63] proposed a model to calculate the atomic strain introduced into the lattice when a solute atom of a different size is introduced into the solvent lattice and suggested that the crystalline lattice becomes destabilized once a critical strain value is exceeded. The volume mismatch was calculated from the relationship:

$$\frac{\Delta V}{V_A} = \frac{V_B - V_A}{V_A} = \left(\frac{r_B}{r_A}\right)^3 - 1 \quad (1)$$

where V and r represent the atomic volume and radius, respectively, the subscripts A and B represent the solvent and solute, respectively, and ΔV represents the difference in atomic volumes between the solute and solvent elements. Since the lattice strain was calculated to increase linearly with solute content, a minimum amount of solute, C_B^{min}, was required for destabilization of the crystalline lattice. It was reported that there is a close relationship between $\frac{\Delta V}{V_A}$ and C_B^{min}according to the equation:

$$\left|\frac{(V_B - V_A)}{V_A}\right| C_B^{min} = 0.1 \quad (2)$$

This concept was later extended to the case of ternary alloy systems [64] and multicomponent systems [65]. The volumetric strain due to solute addition was calculated using the relations:

$$\varepsilon_V^A = \frac{2}{3}\left(\frac{1-2v}{1-v}\right)\lambda_1 \quad (3)$$

where ε_V^A = volumetric strain, λ_1 = mismatch between solute atoms and coordination hole of the nearest neighbor atoms in the multicomponent system, v = Poisson's ratio, and

$$\lambda_1 = \frac{\sum y_i C_i}{1 + \sum C_i(y-1)}\left[\left(\frac{2}{\sum(1+R)}\right)^3 - 1\right] \quad (4)$$

where y is a measure of the deformation required to fit the solute atom B into the hole created by the solvent atom A so that it fits into the A matrix without causing any strain in the matrix. R is the ratio of radii of the solute and solvent atoms, $R_{solute}/R_{solvent}$ and C_i = atomic concentration of the ith element, and y is given by:

$$y = R^3\left[\frac{2}{3}\left(\frac{1-2v}{1-v}\right)\left(\frac{2}{1+R}\right)^3 + \frac{1+v}{3(1-v)}\right] \quad (5)$$

Values of ε_V^A calculated using the above equations for the different alloys with Nb = 1, 2, 4, and 6 at% are shown in Table 4.

It is clear from Table 4 that the absolute value of the critical volume strain is greater than 0.054, the value above which the crystalline lattice becomes destabilized and amorphization occurs. This explains why amorphization has been achieved in all these systems. The negative values of the volumetric strain support the fact that amorphization is accompanied by a contraction of the lattice, which has been demonstrated experimentally. Calculation of the interatomic distance between the transition metal atoms (X_m in Table 4) shows that these values are high for the powder blends containing 2 and 4 at% Nb, thus explaining the ease of destabilization of the crystalline lattice due to topological disorder. The qualitative observation that the width of the peak is larger for the 2 at% Nb blend further lends support to the enhanced GFA at this composition.

The lattice contraction occurring during amorphization can also be understood in terms of the Miracle model relating the atomic diameters of the solvent and solute atoms to the coordination number. In the model of Miracle [66, 67], the solute atoms are surrounded by the solvent atoms. Depending on the atomic radii of the constituent elements, the coordination number is expected to be different. Thus, the coordination numbers are calculated to be 13, 18, 16, and 9 for Ni, Zr, Nb, and B atoms, respectively. Accordingly, the coordination number decreases from 18 to

Table 4 Volumetric strain and interatomic distances between transition metal (TM) atoms in the $Fe_{42}Ni_{28}Zr_{10-x}Nb_xB_{20}$ system; 2θ corresponds to the position of the broad diffuse peak at the time of amorphization and X_m is the average interatomic distance between transition metal atoms

At% Nb	2θ (°)	X_m (nm)	Volumetric strain
1	44.33	0.251	−0.192
2	44.22	0.252	−0.191
4	44.10	0.252	−0.190
6	44.47	0.250	−0.188

16 when the Zr atoms are partially replaced by Nb. This results in a more efficient packing of atoms and less free volume in the matrix, which in turn leads to lattice contraction. Even though different mechanisms for glass formation have been proposed, this is perhaps the first time that clear experimental evidence is provided for some of the proposals.

Other studies

The technique of MA has been successfully employed to synthesize many other advanced materials including photovoltaic materials, supercorroding alloys, energetic materials, and for other applications [13, 14]. We will, however, briefly describe here the special attributes of two materials.

Photovoltaic materials

Copper indium diselenide ($CuInSe_2$)-based photo-voltaic thin-film solar cells continue to receive attention because of their high conversion efficiency [68]. It has been shown that the band gap of $CuInSe_2$ can be modified continuously by substituting Ga for In; the band gap increases with increasing Ga content. For achieving the maximum efficiency of the cell, a Ga/(Ga + In) ratio of 0.3 and a slight deficiency in the copper content have been found to be beneficial.

The $CuInSe_2$-based alloy films are usually obtained either by multisource thermal evaporation and co-deposition or reactive annealing of precursor films. These processes are very involved, contain a number of deposition and annealing steps, pose difficulties in maintaining the desired film composition, and can be expensive. Therefore, we decided to perform band gap engineering through the technique of MA. The two simple steps involved will be synthesis of stoichiometric powder of the $CuIn_{0.7}Ga_{0.3}Se_2$ (CIGS) alloy by MA and obtain the bulk target by hot isostatic pressing of the milled powder. Milling of the blended elemental powder was conducted in a Fritsch Pulverisette P5 mill using a copper container and copper grinding balls at two different milling speeds and at two different BPR values.

Milling of the powders even for a short time resulted in the formation of the desired $CuIn_{0.7}Ga_{0.3}Se_2$ phase. For example, by milling at a BPR of 20:1 and a speed of 300 rpm, the tetragonal $CuIn_{0.7}Ga_{0.3}Se_2$ phase had formed. But, small amounts of other phases were also present at this stage. However, on continued milling of this powder for 20 min, only the tetragonal $CuIn_{0.7}Ga_{0.3}Se_2$ phase had formed homogeneously [69]. This phase could be indexed on the basis of a tetragonal structure with the lattice parameters $a = 0.5736$ nm, $c = 1.1448$, and $c/a = 1.9958$ having the space group $I\bar{4}2d$. Even though the quaternary Cu–In–Ga–Se tetragonal phase exists over a wide composition range, the present XRD pattern could be most satisfactorily indexed on the basis of the tetragonal phase with the stoichiometry $CuIn_{0.7}Ga_{0.3}Se_2$. Scherrer analysis of the peak widths confirmed that the crystallite size reached a saturation value of about 8 nm [70]. The phase identification and crystallite size determination were confirmed by transmission electron microscopy (TEM) studies [71].

The results of chemical analysis of the milled powder under different milling conditions are presented in Table 5. It is clear that the composition of the milled powder is reasonably close to the targeted composition. But, because some copper has been picked up from the container and/or the grinding balls during milling, the copper content appears to be higher than what the stoichiometry requires. But, the powder milled at a BPR of 10:1 and a speed of 150 rpm for 40 min did not pick up much copper. Consequently, the chemical composition of the powder milled under these conditions is quite close to the starting powder mixture. By further optimizing the powder processing conditions (BPR, speed of rotation, and time of milling), it is possible to control the composition of the final powder to the exact desired value. Hot pressing of the MA powder at 750 °C and 100 MPa for 2 h produced a fully dense material.

This investigation clearly proves that it is possible to obtain the CIGS targets of the required stoichiometry through a combination of MA and hot isostatic pressing or vacuum hot pressing. Further, it is possible to control the stoichiometry by optimizing the MA process parameters. Such an approach should be equally applicable to synthesize other target materials.

Combustion studies of metal particles

One of the potential applications for materials with fine grain sizes is in improving the combustion characteristics of propellants [72]. It is known that Mg can be easily combusted, but it has a low heat content (14.9 MJ/kg). On the other hand, Al has a higher heat content (32.9 MJ/Kg), but is more difficult to combust. Therefore, it was decided to see if Al and Mg can be alloyed together to increase the

Table 5 Chemical analysis (at%) of the Cu–In–Ga–Se powder mechanically alloyed under different processing conditions [50]

BPR	Speed (rpm)	Time (min)	Cu	In	Ga	Se
20:1	300	120	32.61	15.23	6.53	45.62
10:1	300	240	31.73	15.63	6.71	45.93
10:1	150	40	25.98	16.98	7.25	49.78
Targeted ($Cu_{0.97}In_{0.7}Ga_{0.3}Se_2$)			24.43	17.63	7.56	50.38

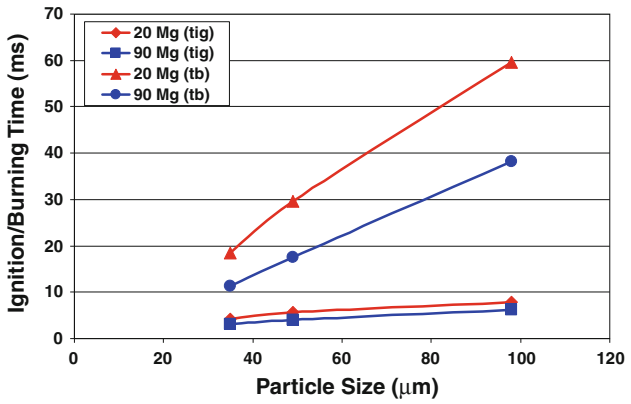

Fig. 10 Ignition time, τ_{ig} and burning time, τ_b as a function of particle size for two different alloy compositions (Al-20 at% Mg and Al-90 at% Mg)

net heat content and also be able to combust relatively easily. Accordingly, a series of Al–Mg powder blends of different compositions were mechanically alloyed in a SPEX mill. Since the milled powder normally contains a range of particle sizes, the milled powder was sieved to well-defined particle sizes in the ranges of 20–25 μm, 45–53 μm, and 90–106 μm. These powder particles were then burned in a methane-air premixed flame on a Meeker burner, at a temperature of approximately 1,800 K. Burning of the powder particles was recorded using chopped images by long-exposure digital photography. Knowing the rotational speed of the chopper and the number of exposures per revolution, the burning time, τ_b and the ignition time, τ_{ig} could be determined. Figure 10 shows the plot of variation of τ_{ig} and τ_b with particle size for two different alloy compositions (Al-20 at% Mg and Al-90 at% Mg) [73]. It is clear from this plot that both the ignition and burning times decrease with (a) a decrease in particle size and (b) an increase in Mg content. Thus, by a judicious choice of particle size and alloy composition, it should be possible to control the ignition and burning times.

Conclusions

Mechanical alloying has been shown to be a very versatile and useful method in synthesizing a variety of advanced materials under equilibrium and non-equilibrium conditions. But, large-scale applications require materials that could be produced in tonnage quantities, and materials that have been well characterized and exhibit reproducible properties. However, the bane of MA has been the three Cs—Cost, Consolidation, and Contamination. Powder processing is expensive and therefore, unless one is able to identify niche markets for the MA products and the powders produced in large volumes, cost is likely to continue to be high. In some cases, e.g., hydrogen storage materials or magnetic alloys, the high cost may be acceptable in view of the improved properties and enhanced performance. We have presented two clear examples of synthesizing nanocomposites in Al–Al_2O_3 and TiAl–Ti_5Si_3 systems containing a high volume fraction of the reinforcement phase and bulk metallic glass alloy compositions in Fe-based alloys. Apart from successfully synthesizing these materials, these studies have also provided a scientific basis for understanding the load partitioning behavior and superplastic forming of the nanocomposites, and criteria and mechanism of glass formation in the Fe-based alloy systems.

Acknowledgements The study reported here is supported by the US National Science Foundation under grants DMR-0314212 and DMR-0334544 and by the Office of Naval Research. The authors also acknowledge fruitful collaboration and useful discussions with Drs. Raj Vaidyanathan, Linan An, and Ruey-Hung Chen of the University of Central Florida, Orlando, USA, Professor Rüdiger Bormann of the Hamburg-Harburg Technical University, Hamburg, Germany, and Dr. S.J. Hong of Kongju National University, Kongju, South Korea. C.S. is also thankful to the experimental input from his graduate students—Pushkar Katiyar, Balaji Prabhu, Satyajeet Sharma, Devender Singh, and UMR Seelam, all from the University of Central Florida.

References

1. Bloor D, Brook RJ, Flemings MC, Mahajan S (eds) (1994) The encyclopedia of advanced materials. Pergamon, Oxford, p xi
2. Anantharaman TR, Suryanarayana C (1987) Rapidly solidified metals: a technological overview. Trans Tech Publications, Zurich, Switzerland
3. Liebermann HH (ed) (1993) Rapidly solidified alloys: processes, structures, properties, applications. Marcel Dekker, New York, NY
4. Suryanarayana C, Inoue A (2011) Bulk metallic glasses. CRC Press, Boca Raton, FL
5. Suryanarayana C, Jones H (1988) Int J Rapid Solidif 3:253
6. Trebin HR (ed) (2003) Quasicrystals: structure and physical properties. Wiley-VCH, Weinheim
7. Suryanarayana C (1995) Int Mater Rev 40:41
8. Gleiter H (2000) Acta Mater 48:1
9. Suryanarayana C (2007) Adv Eng Mater 7:983
10. Turnbull D (1981) Metall Trans A 12:695
11. Suryanarayana C (ed) (1999) Non-equilibrium processing of materials. Pergamon, Oxford
12. Benjamin JS (1990) Metal Powder Report 45:122
13. Suryanarayana C (2001) Prog Mater Sci 46:1
14. Suryanarayana C (2004) Mechanical alloying and milling. Marcel Dekker, New York, NY
15. Takacs L (2002) Prog Mater Sci 47:355
16. Suryanarayana C (1995) Bibliography on mechanical alloying and milling. Cambridge International Science Publishing, Cambridge, UK
17. Clyne TW, Withers PJ (1995) An introduction to metal matrix composites. Cambridge University Press, Cambridge, UK
18. Kim HM, Kim TS, Suryanarayana C, Chun BS (2000) Mater Sci Eng A 287:59
19. Son HT, Kim TS, Suryanarayana C, Chun BS (2003) Mater Sci Eng A 348:163

20. Hong SJ, Kim HM, Huh D, Suryanarayana C, Chun BS (2003) Mater Sci Eng A 347:198
21. Prabhu B, Suryanarayana C, An L, Vaidyanathan R (2006) Mater Sci Eng A 425:192
22. Klassen T, Bohn R, Suryanarayana C, Fanta G, Bormann R (2003) In: Shaw L, Suryanarayana C, Mishra RS (eds) Processing and properties of structural nanomaterials. TMS, Warrendale, PA, p 93
23. Klassen T, Suryanarayana C, Bormann R (2008) Scripta Mater 59:455
24. Suryanarayana C, Behn R, Klassen T, Bormann R (2010) (submitted)
25. Mohan P, Suryanarayana C, Desai V (2004) In: Bandyopadhyay S et al (eds) Nanomaterials: synthesis, characterisation, and application. Tata McGraw-Hill Publ. Co. Ltd., New Delhi, India, p 171
26. Suryanarayana C (2008) Mater Sci Eng A 479:23
27. Al-Aqeeli N, Mendoza-Suarez G, Suryanarayana C, Drew RAL (2008) Mater Sci Eng A 480:392
28. Wang Y, Suryanarayana C, An L (2005) J Am Ceram Soc 88:780
29. Prabhu B (2005) MS Thesis, University of Central Florida, Orlando, USA
30. Nguyen TT, Suryanarayana C, Vaidyanathan R (2010) Unpublished results, University of Central Florida, Orlando, FL, USA
31. Froes FH, Suryanarayana C, Eliezer D (1992) J Mater Sci 27:5113. doi:10.1007/BF02403806
32. Appel F, Wagner R (1998) Mater Sci Eng Reports R22:187
33. Oehring M, Appel F, Pfullmann T, Bormann R (1995) Appl Phys Lett 66:941
34. Bohn R, Klassen T, Bormann R (2001) Intermetallics 9:559
35. Mishra RS, Lee WB, Mukherjee AK, Kim Y-W (1995) In: Kim Y-W, Wagner R, Yamaguchi M (eds) Gamma titanium aluminides. TMS, Warrendale, PA, p 571
36. Suryanarayana C (1984) Bull Mater Sci India 6:579
37. Luborsky FE (ed) (1983) Amorphous metallic alloys. Butterworths, London
38. Inoue A (2000) Acta Mater 48:279
39. Suryanarayana C, Seki IR, Inoue A (2009) J Non-Cryst Solids 355:355
40. Suryanarayana C, Norton MG (1998) X-ray diffraction: a practical approach. Plenum, New York, NY
41. Massalski TB (ed) (1986) Binary alloy phase diagrams. ASM International, Materials Park, OH
42. de Boer FR, Boom R, Mattens WCM, Miedema AR, Niessen AK (1988) Cohesion in metals. Transition metal alloys. North-Holland, Amsterdam
43. Sharma S, Vaidyanathan R, Suryanarayana C (2007) Appl Phys Lett 90:111915-1
44. Cho YS, Koch CC (1993) J Alloys Compd 194:287
45. Froes FH, Suryanarayana C, Russell KC, Li CG (1995) Mater Sci Eng A 192/193:612
46. Klassen T, Oehring M, Bormann R (1997) Acta Mater 45:3935
47. Stoloff NS, Davies RG (1968) Prog Mater Sci 13:1
48. Turnbull D (1969) Contemp Phys 10:473
49. Wong R, Merz MD (1976) Nature (London) 260:35
50. Seelam UMR, Suryanarayana C (2006) Unpublished results, University of Central Florida, Orlando, FL
51. Nose M, Masumoto T (1980) Sci Rep Res Inst Tohoku Univ A 28:135
52. Köster U, Herold U (1981) In: Güntherodt HJ, Beck H (eds) Glassy metals I. Springer-Verlag, Berlin, p 225
53. Patil U, Hong SJ, Suryanarayana C (2005) J Alloys Compd 389:121
54. Sharma S, Suryanarayana C (2007) J Appl Phys 102:083544-1
55. Sharma S, Suryanarayana C (2008) J Appl Phys 103:013504-1
56. Trudeau ML, Schulz R, Dussault D, Van Neste A (1990) Phys Rev Lett 64:99
57. Suryanarayana C (1995) Intermetallics 3:153
58. Blatter A, Von Allmen M (1985) Phys Rev Lett 54:2103
59. Park ES, Kim DH (2006) Acta Mater 54:2597
60. Ma E (2006) Prog Mater Sci 50:413
61. Miedema AR, de Boer FR, Boom R (1997) CALPHAD 1:341
62. Sharma S, Suryanarayana C (2008) Scripta Mater 58:508
63. Egami T, Waseda Y (1984) J Non-Cryst Solids 64:113
64. Yan ZJ, Li JF, He SR, Zhou YH (2003) Mater Res Bull 38:681
65. Egami T (2003) J Non-Cryst Solids 317:30
66. Miracle DB (2004) Nat Mater 3:697
67. Miracle DB (2006) Acta Mater 54:4317
68. Birkmire RW, Eser E (1997) Ann Rev Mater Sci 27:625
69. Suryanarayana C, Ivanov E, Noufi R, Contreras MA, Moore JJ (1999) J Mater Res 14:377
70. Ivanov E, Suryanarayana C (2008) In: 23rd European photovoltaic solar energy conference, September 1–5, 2008, Valencia, Spain, p 2513
71. Suryanarayana C, Ivanov E, Noufi R, Contreras MA, Moore JJ (1998) Thin Solid Films 332:340
72. Dreizin EL (2000) Prog Energ Combust Sci 26:57
73. Chen RH, Suryanarayana C, Chaos M (2006) Adv Eng Mater 8:563